TÜBİTAK

Turkish Journal of Physics

http://journals.tubitak.gov.tr/physics/

Research Article

Turk J Phys
(2019) 43: 11 – 25
© TÜBİTAK
doi:10.3906/fiz-1802-26

Effects of cooling rate on the atomic structure and glass formation process of $Co_{90}Zr_{10}$ metallic glass investigated by molecular dynamics simulations

Murat ÇELTEK[1,*], **Sedat ŞENGÜL**[2]
[1]Faculty of Education, Trakya University, Edirne, Turkey
[2]Department of Physics, Faculty of Science, Trakya University, Edirne, Turkey

Received: 15.02.2018 • **Accepted/Published Online:** 07.12.2018 • **Final Version:** 22.02.2019

Abstract: In this study, the atomic structure and the glass formation process of $Co_{90}Zr_{10}$ metallic glass alloy were studied by molecular dynamic simulation based on the embedded atom method using four different cooling rates. The average atomic volume and the potential energy of the system were observed to be strongly dependent on the cooling rate during rapid solidification, and the glass transition temperature decreased with decreasing cooling rate. The radial distribution functions and the structure factors derived from molecular dynamics simulations at 300 K agreed well with the experimental and other molecular dynamics results. The coordination numbers calculated at 300 K were consistent with the experimental results in the literature. The local structural atomic orders of the system have been characterized by Honeycutt–Andersen indices and the Voronoi tessellation method. We realized that the FCC and icosahedral short-range order increases with decreasing cooling rate, the icosahedral clusters are predominant in the $Co_{90}Zr_{10}$ metallic glass, and the fraction of the icosahedral polyhedra increases with decreasing cooling rate and temperature. We have seen that Co-centered Voronoi polyhedrals such as $\langle 0,2,8,2\rangle$, $\langle 0,0,12,0\rangle$, and $\langle 0,1,10,2\rangle$ play a dominant role in the development of the icosahedral order of the $Co_{90}Zr_{10}$ alloy.

Key words: Metallic glassy, glass transition temperature, short-range order, molecular dynamic simulations, icosahedral, Honeycutt–Andersen index, Voronoi tessellation

1. Introduction

Metallic glasses (MGs) have been widely used due to their interesting structural, electronic, and magnetic properties [1–3] since the discovery of the first MG of $Au_{75}Si_{25}$ [4]. The speed of cooling applied to a liquid melt is one of the most important parameters for producing MG from that melt. It is well known that the atomic rearrangement is impeded in liquid alloys with high viscosity. The hindering of crystallization is possible by freezing the disordered positions of the atoms in the liquid. The temperature at which the system becomes solid is called the glass transition temperature (T_g) of the system. In the last four decades, the discovery of rapidly solidified alloys and large-scale investigations conducted on them have revealed new things in basic and applied magnetism. Although there are numerous technological applications of the bulk metallic MGs, the links between the structural and magnetic properties of these systems are not yet fully understood. Furthermore, it is well known that these properties are strongly dependent on the atomic short-range order (SRO) [5]. The interesting and unique physical properties of amorphous alloys are determined by the spatial arrangement of atoms and the chemical interactions between atoms. Co-rich $Co_{1-x}Zr_x$ alloys have been experimentally studied

*Correspondence: mceltek@trakya.edu.tr

This work is licensed under a Creative Commons Attribution 4.0 International License.

by many researchers due to their strong ferromagnetic [6,7] and interesting physical properties. A crystallization study of $Co_{1-x}Zr_x$ amorphous alloys prepared at a wide range of 8% to 80% Zr concentration was performed by Mohammed Idrus and Grundy [8] using the sputtering method. Babanova et al. [9] used extended X-ray absorption fine structure (EXAFS) spectra for Co and Zr K absorption edges and X-ray scattering data together to obtain information on the SRO of the amorphous $Co_{90}Zr_{10}$ binary alloy. They observed that in the amorphous $Co_{90}Zr_{10}$ alloy produced by melt spinning, the chemical ordered with Co-Co and Co-Zr bonds dominate and the distance of Co-Zr was shorter than the crystal value. The phases, microstructures, and magnetic properties of $Co_{90-x}Zr_{10+x}$ (x = 0-20) alloys were investigated by Saito [10] using X-ray diffraction, a scanning electron microscope, and a vibrating sample magnetometer, respectively.

Although some experimental and simulation work has been done to study the liquid and amorphous structure of Co-Zr alloys, there is still a deep inadequacy in terms of the nature of the local structure of Co-Zr alloys at the Co-rich side. The aim of this work is to investigate the cooling rate effects on the ordered atomic structure, especially the icosahedral SRO, and the structural evolution of $Co_{90}Zr_{10}$ liquid and amorphous alloy using molecular dynamics (MD) simulations in conjunction with the embedded atom method (EAM) of Daw and Baskes [11]. Based on MD-EAM calculations, we obtain the radial distribution functions (RDFs), the structure factors (SFs), and the coordination numbers (CNs), and furthermore we analyze the SRO in liquid and amorphous systems by Honeycutt–Andersen (HA) and Voronoi tessellation (VT) analysis methods. As a result, we can better define the local configurations in the system. It is expected that these results will be useful for understanding the local atomic structure, glass transition, and SRO of the Co-Zr system during the cooling process.

2. Interatomic potential and computational procedure

The reliability of MD simulation depends on the interatomic potential that can explain better the atomic interactions of the system. In the present study, the EAM potential was adopted to simulate $Co_{90}Zr_{10}$ binary metallic liquid and glass. In the EAM, the total energy of an N-atom system has the following form [11]:

$$E_{tot} = \frac{1}{2} \sum_{i,\, j,\, i \neq j} \varphi_{ij}(r_{ij}) \; + \; \sum_{i} F_i\left(\rho_i\right), \tag{1}$$

where $\varphi_{ij}(r_{ij})$ is the pair interaction energy between atoms i and j separated by distance r_{ij} and F_i is the embedding energy associated with embedding an atom i into a local site with electron density ρ_i. The local electron density, ρ_i, can be calculated using:

$$\rho_i = \sum_{j,\, j \neq i} f_j\left(r_{ij}\right), \tag{2}$$

where $f_j(r_{ij})$ is the electron density contribution from atom j at the site of atom i. The EAM potential for an alloy does not contain only the three functions, ϕ, ρ, and F for each of the constituent elements; it also includes the ϕ^{AB} pair energy between elements A and $B(A \neq B)$. The generalized elemental pair potential form of the EAM alloy model used in this study can be expressed as follows [12]:

$$\varphi\left(r\right) = \frac{A \exp\left[-\alpha\left(r/r_e - 1\right)\right]}{1 + \left(r/r_e - \kappa\right)^{20}} - \frac{B \exp\left[-\beta\left(r/r_e - 1\right)\right]}{1 + \left(r/r_e - \lambda\right)^{20}}, \tag{3}$$

where A,B, α, and β are adjustable parameters; r is the spacing between the two atoms; r_e is the equilibrium spacing between nearest neighbors, and κ and λ are two additional parameters. The electron density function can be expressed as:

$$f(r) = \frac{f_e \exp\ [-\beta (r/r_e - 1)]}{1 + (r/r_e - \lambda)^{20}}. \tag{4}$$

The new form of pair potential for dissimilar species can be expressed as:

$$\varphi^{AB}(r) = \frac{1}{2}\left[\frac{f^B(r)}{f^A(r)}\varphi^{AA}(r) + \frac{f^A(r)}{f^B(r)}\varphi^{BB}(r)\right]. \tag{5}$$

The forms of embedding energy functions equipped for working well over a wide range of electron density can be expressed as follows:

$$F(\rho) = \sum_{i=0}^{3} F_{ni}\left(\frac{\rho}{\rho_n} - 1\right)^i, \quad \rho < \rho_n, \quad \rho_n = 0.85\rho_e, \tag{6}$$

$$F(\rho) = \sum_{i=0}^{3} F_i\left(\frac{\rho}{\rho_n} - 1\right)^i, \quad \rho_n < \rho < \rho_0, \quad \rho_0 = 1.15\rho_e, \tag{7}$$

$$F(\rho) = F_e\left[1 - \ln\left(\frac{\rho}{\rho_s}\right)^n\right]\left(\frac{\rho}{\rho_s}\right)^n, \quad \rho_0 \leq \rho. \tag{8}$$

The parameters for EAM potential functions are listed in Table 1 and the details can be seen in Ref. [12].

Table 1. Model parameters for the Zr and Co metals [12].

Metal	r_e (Å)	f_e	ρ_e	ρ_s	α
Zr	3.199 978	2.230 909	30.879 991	30.879 991	8.559 190
Co	2.505 976	1.975 299	27.206 789	27.206 789	8.679 625
	β	A (eV)	B (eV)	κ	λ
Zr	4.564 902	0.424 667	0.640 054	0.5	1.0
Co	4.629 134	0.421 378	0.640 107	0.5	1.0
	F_{n0} (eV)	F_{n1} (eV)	F_{n2} (eV)	F_{n3} (eV)	F_0 (eV)
Zr	–4.485 793	–0.293 129	0.990 148	–3.202 516	–4.51
Co	–2.541 799	–0.219 415	0.733 381	–1.598 003	–2.56
	F_1 (eV)	F_2 (eV)	F_3 (eV)	η	F_e (eV)
Zr	0	0.928 602	–0.981 870	0.597 133	–4.509 025
Co	0	0.705 845	–0.687 140	0.694 608	–2.559 307

In this work, MD simulations were performed with a system consisting of 8192 atoms (7373 Co atoms and 819 Zr atoms) under three-dimensional periodic boundary conditions and using open source code DL_POLY [13]. The interatomic interactions of $Co_{90}Zr_{10}$ binary MG were described by the potential of the EAM provided by Zhou et al. [12]. The time step was chosen to be 1 fs, which was a sufficiently small value to reduce the fluctuations of the total energy. The temperature and pressure were controlled using a Berendsen thermostat

and barostat. The motion equations were solved by Verlet leapfrog algorithm with a time step of 1×10^{-15} s. During the MD simulation, the model alloy system was first run with 5,000,000 MD steps at 2500 K under pressure of 0 Pa to obtain an equilibrium liquid phase for the initial configuration. Then the liquid system was cooled with different cooling rates ($Q_1 = 10$ K ps^{-1}, $Q_2 = 1$ K ps^{-1}, $Q_3 = 0.1$ K ps^{-1}, and $Q_4 = 0.01$ K ps^{-1}) from 2500 to 300 K with an increment of 50 K, and in the following sections, we show only the results between 2000 K and 300 K to avoid repetition. In the next sections of this paper, we will discuss the results obtained from the slower cooling rate of $Q_4 = 0.01$ K ps^{-1} in detail.

3. Results and discussion

3.1. Glass formation

In order to investigate the effects of the cooling rate on the glass-forming ability (GFA) and atomic structure of $Co_{90}Zr_{10}$ alloy, we have used different cooling rates from $Q_1 = 10$ to $Q_4 = 0.01$ K ps^{-1}. Figure 1 shows the variation of the average atomic volume V of $Co_{90}Zr_{10}$ alloy as a function of temperature under four cooling rates ($Q_1 = 10$ K ps^{-1}, $Q_2 = 1$ K ps^{-1}, $Q_3 = 0.1$ K ps^{-1}, and $Q_1 = 0.01$ K ps^{-1}). The change in the slope of the average atomic volumes at low and high temperatures indicates the glass transition of this alloy for the four cases studied. Although there is no difference between the four curves at high temperatures, the difference becomes more pronounced depending on the cooling rate as the temperature decreases. The overlap at high temperatures indicates that the atoms can move rapidly enough at all cooling rates due to temperature variations. As the simulation time is long enough, it can be seen from Figure 1 that the system's volume changes to lower values at low temperatures during the cooling processes. With decrease in the temperature, the volume gradually decreases and an inflection point corresponding to the glass transition temperatures (T_g) is formed between the low and high temperature regions. The inset in the lower right corner of Figure 1 illustrates the values of the average atomic volume fitted to a linear function to estimate T_g at cooling rate $Q_4 = 0.01$ K ps^{-1}. For the other three cooling rates, the T_g values have been determined using the same method and the changes in T_g depending on the cooling rate are exhibited in Figure 2a. In our simulation, we observed a systematic relationship between the T_g values and the cooling rate; that is, T_g (from 964 K to 833 K) decreased with decreasing cooling rate (from $Q_1 = 10$ K ps^{-1} to $Q_4 = 0.01$ K ps^{-1}). Furthermore, the linear variation of T_g with logQ and the increase in T_g with increasing cooling rate reveal that glassy transition is indeed a typical kinetic process [14–16]. The higher cooling rate used in the simulation gives a shorter time to relax the system, thus leading to higher T_g values during liquid–glass transition.

As the cooling rate increases, the volume and total energy increase as well; the curves of these two variables as functions of cooling are depicted in Figures 2b and 2c. According to free-volume theory [17], when a liquid system is cooled rapidly to obtain an amorphous structure, the excess free volume in the liquid will be trapped in the glassy state. The cooling system with $Q_4 = 0.01$ K ps^{-1} cooling rate has a relatively lower volume and energy value than the cooling systems with other cooling rates ($Q_1 = 10$ K ps^{-1}, $Q_2 = 1$ K ps^{-1}, and $Q_3 = 0.1$ K ps^{-1}), indicating that the final amorphous system has a more closely packed structure than the others. The higher the cooling rate for a system, the greater the free volume will be in the newly formed MG system. If we look at it from a different point of view, a slower cooling rate allows more time to equilibrate the system, thus preventing the formation of more free volume.

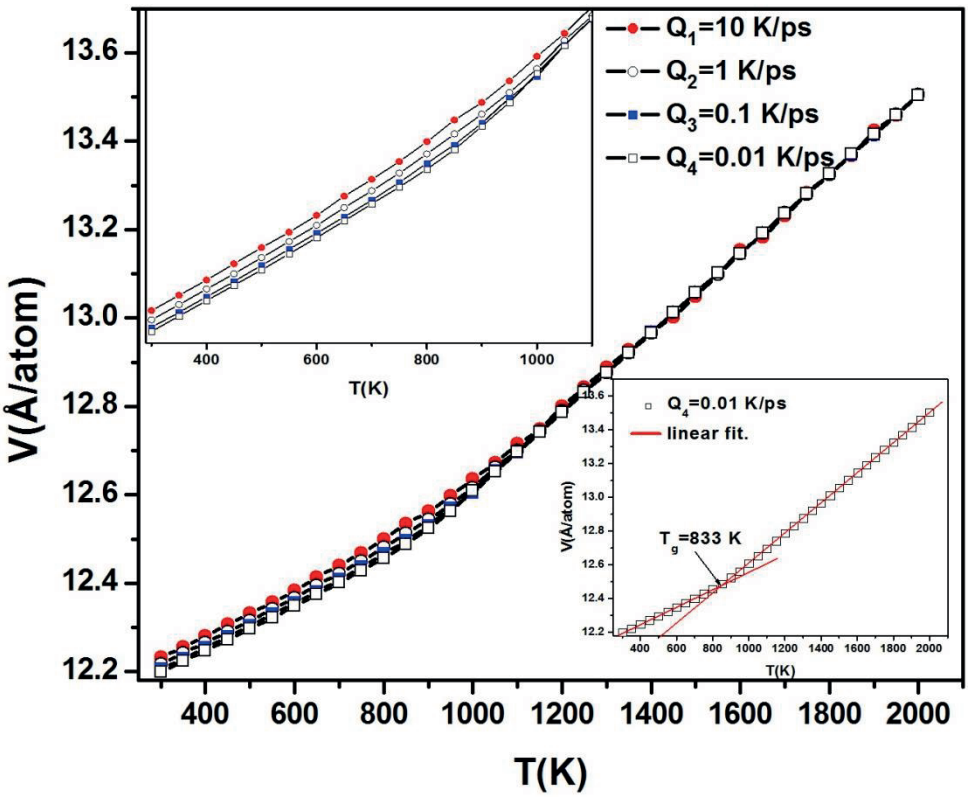

Figure 1. Temperature dependence of volume at four cooling rates for the $Co_{90}Zr_{10}$ alloy. The top left and bottom right insets are the volume as a function of the temperature from 1100 to 300 K and the volume fitted to a linear function to estimate the T_g at cooling rate of $Q_4 = 0.01$ K ps^{-1}, respectively.

3.2. Radial distribution functions and structure factors

RDF and SF analysis are among the most important methods used to reveal the structural properties of a system, especially for liquid, amorphous, and crystalline structures. The partial RDF (PRDF) for atom α and atom β is calculated as [18]:

$$g_{\alpha\beta}(r) = \frac{V}{N_\alpha N_\beta} \left\langle \sum_i^N \sum_{j \neq i}^N \delta\left(r - r_{ij}\right) \right\rangle, \tag{9}$$

where V is the volume of the simulation box and N_α and N_β are the number of atoms of type α and type β, respectively. The static SF, S(Q), is defined through a Fourier transformation of g(r) as:

$$S(q) = 1 + 4\pi\rho \int_0^\infty r^2 \frac{\sin qr}{qr} \left(g\left(r\right) - 1\right) dr. \tag{10}$$

The SF characterizes the spatial distributions of the atoms in the system and provides a signature of the spatial structure. The SF for the simulated $Co_{90}Zr_{10}$ MG using the cooling rate of $Q_4 = 0.01$ K ps^{-1} at 300 K is obtained by means of the Fourier transformation of the total RDF and is presented in Figure 3 together with experimental data [9]. The inset is a snapshot of the simulations box at 300 K. It can be seen that our results agree well with the experiment. This is an indication that the EAM potential can quite well describe

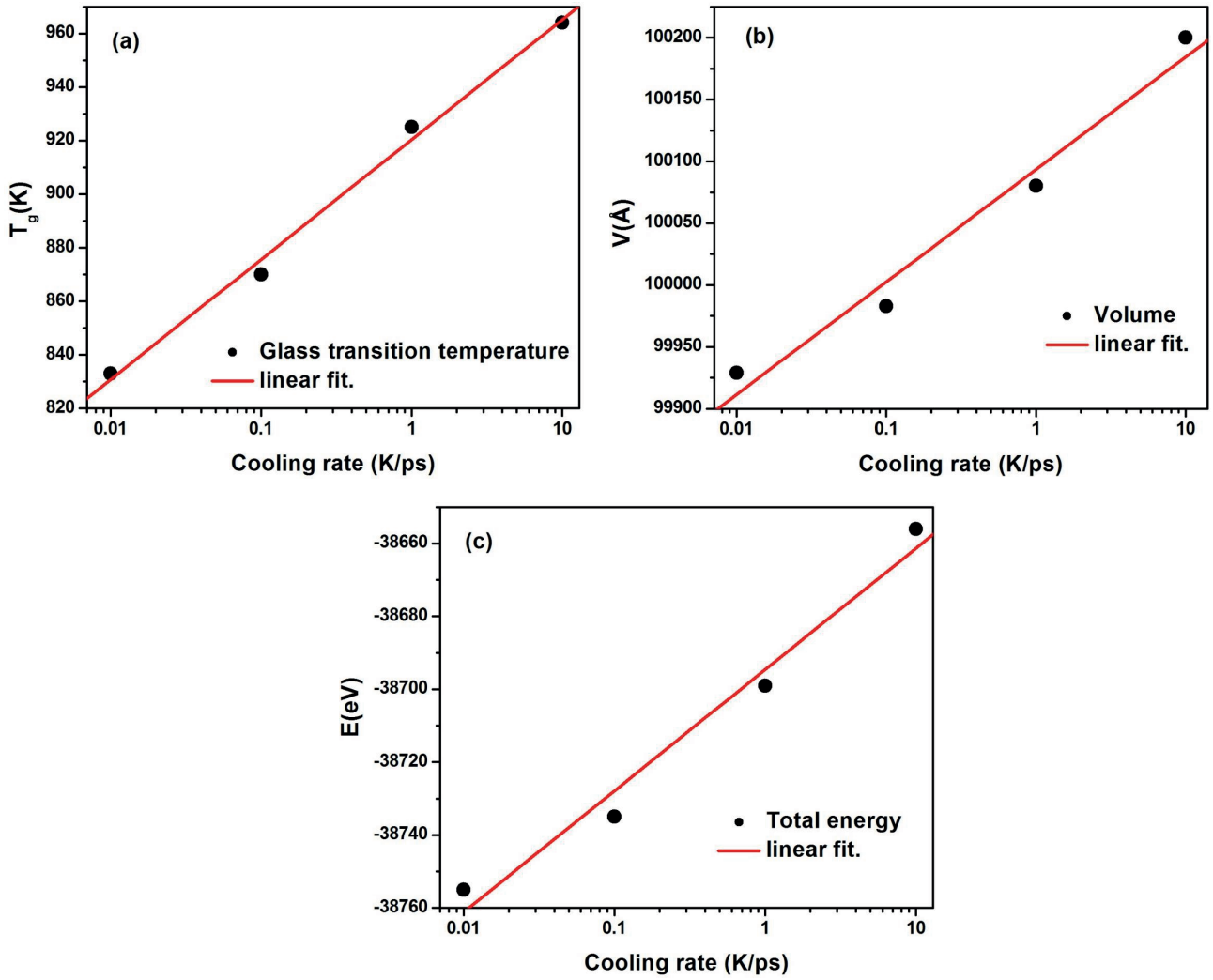

Figure 2. The T_g, volume, and total energy of $Co_{90}Zr_{10}$ amorphous state change as a function of cooling rate: (a) T_g, (b) volume at 300 K, and (c) total energy at 300 K.

the atomic interactions in the studied system. An agreement with the splitting of the second maximum peaks of the simulated and experimental SF curves has been observed, which is known as a characteristic feature for MGs.

We analyzed the RDF, g(r), to investigate the structural properties of the system during the cooling process, which is widely used to describe the structural characteristics of liquid, amorphous, and solid structures [15,19,20]. Figure 4 presents the total RDF curves obtained at 300 K with four different cooling rates. The insets are presented to see the details of the changes in the peak points of the first and second peaks of the total RDF curves. The first peaks of the RDF curves are at nearly the same position for all glasses. Furthermore, all the second peaks have a splitting specific to amorphous alloys. These splittings depict that some SRO and/or medium-range order (MRO) is developing within the system during the cooling process [19,21,22].

The total RDF curves simulated for some selected temperatures between 2000 K and 300 K with the cooling rate of Q4 = 0.01 K ps^{-1} are given in Figure 5. During cooling, the RDF curves at high temperatures exhibit typical behavior of the liquid structure. We observe that the system is still in the structure of liquid,

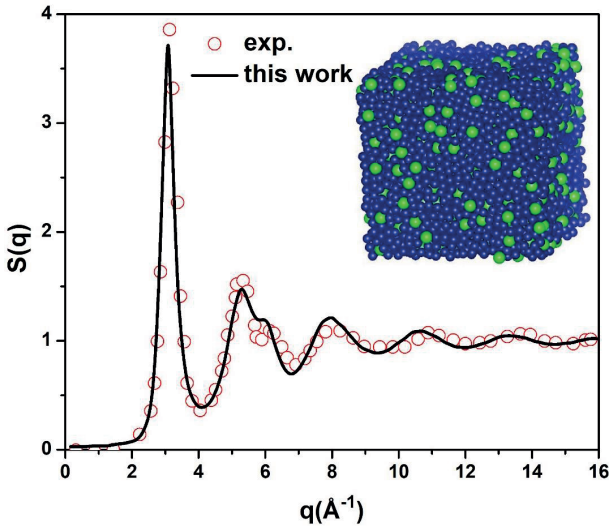

Figure 3. Total SF of experimental [9] and simulated amorphous $Co_{90}Zr_{10}$ using the cooling rate of $Q_4 = 0.01$ K ps^{-1} at 300 K. The inset is a snapshot of the simulations box at 300 K. Blue and green atoms represent Co and Zr atoms, respectively.

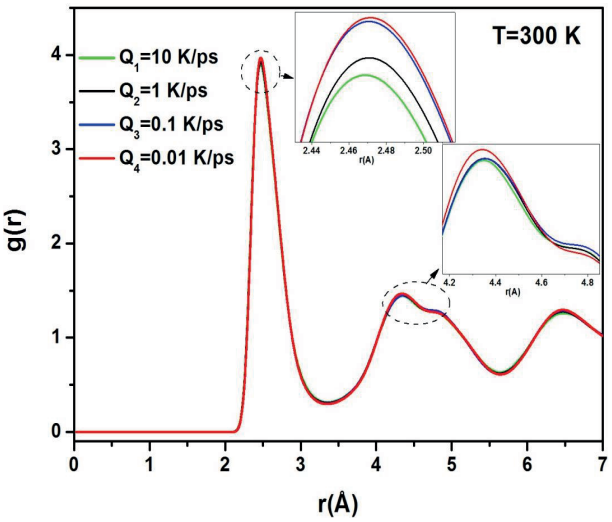

Figure 4. The total RDF curves under various cooling rates for the $Co_{90}Zr_{10}$ MG at 300 K. The insets represent a closer representation of the first and second peaks of the total RDF curves.

although the system cooled to 1000 K is actually a supercooled liquid. The height of the first peaks of total RDFs increases with decreasing temperature, which is an indication that the atomic order in the first coordination shell increases with decreasing temperature. The second peak of total RDF starts to split at 900 K and this splitting becomes more pronounced with decreasing temperature. In addition, this splitting is a characteristic feature of glassy systems, indicating that the system is in the amorphous state at low temperatures.

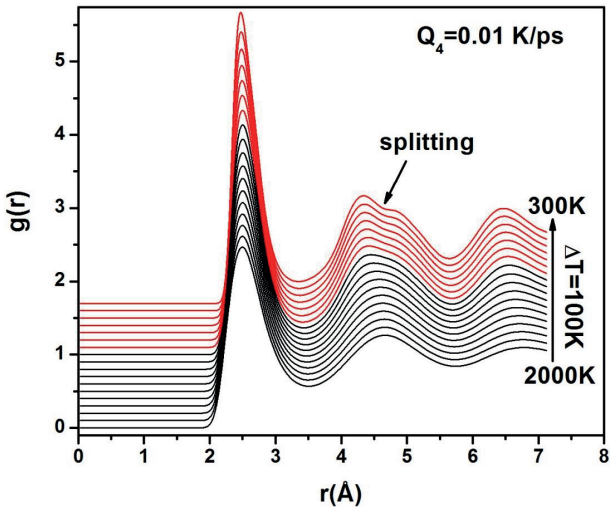

Figure 5. The total RDF curves of the $Co_{90}Zr_{10}$ alloy at different temperatures under cooling rate of $Q_4 = 0.01$ K ps^{-1}.

The PRDF expresses the spatial correlations among different types of atoms and allows us to obtain more information about what happens between atoms in the system. Although PRDFs are difficult to obtain directly from the experiment, they can be easily calculated in MD simulations. The PRDFs of the amorphous

$Co_{90}Zr_{10}$ alloy simulated at 300 K are exhibited comparatively in Figures 6a–6c with the experimental [9] and theoretical data [23] in the literature. The simulated PRDFs of Co-Co and Co-Zr pairs, excluding the Zr-Zr pair, for $Co_{90}Zr_{10}$ glass at 300 K are in good agreement with the experimental [9] and other MD simulations [23] results. The splitting of the second peaks for all pairs at 300 K gives further evidence of the formation of the $Co_{90}Zr_{10}$ glass. As can be noticed in Figure 6c, experimental PRDFs for the Zr-Zr pairs are different from the common $g_{ij}(r)$ behavior, the cause of which was reported previously by Babanov et al. [9]: the experimental Zr-Zr PRDFs do not exhibit a structural trend and are predicted as a possible lack of resolution in X-ray diffraction and EXAFS due to the fact that they contribute little in the spectra of these minority atoms [23]. Although our simulated results for the Zr-Zr pairs are not consistent with the experimental results, they appear to be more consistent with the MD results simulated by Rößler and Teichler [23]. From other MD simulations and our results, it is seen that the second maximum peaks of the PRDFs are much higher and stronger than the first maximum peaks. This case is an indication that Zr atoms do not prefer to cluster in the glassy state. Compared to other MD results, the position of the first maximum peak of our PRDF curve is more consistent with the experimental PRDF curve. As a result, it seems that the resolution of these methods cannot solve any structure of the Zr-Zr pair correlations because of the low contribution of minority Zr atoms in the $Co_{90}Zr_{10}$ alloy.

3.3. Coordination numbers (CNs)

The CN helps us to get more information about the statistical description and short-range correlations of the nearest-neighbor atoms in liquid and amorphous systems. By using the data of total and partial RDFs, we can calculate the total and partial CNs in the first neighboring shell by integrating g(r) and $g_{ij}(r)$:

$$N_{ij} = \int_0^{r_{\min}} 4\pi r^2 \rho_j g_{ij}(r)\, dr, \tag{11}$$

where ρ_j is the density of atom j and r_{min} is the first minimum of $g_{ij}(r)$.The total CN for atom i is calculated as $CN_i = \sum_j N_{ij}$. The calculated results are presented in Table 2 together with the experimental results in the literature. Our results are consistent with experimental ones [9]. The CNs around the Zr atoms (N_{Zr} =15.80) are larger than that around the Co atoms (N_{Co} =12.64). This difference between the CNs is due to the difference in atomic sizes of the Zr (R_{Zr} = 1.60 Å) and Co (R_{Co} = 1.25 Å) atoms. These results are also consistent with those we obtained using different interatomic potentials for the Zr-Co-Cu alloy [24].

3.4. Honeycutt–Andersen bond-type indices

The CN reflects the statistical average of the atomic distribution in the system, but it cannot describe the local atomic configuration. We used the Honeycutt–Andersen (HA) [25] bond-type index to describe the local configurations of liquid and amorphous systems. This method allows the classification of some specific groupings such as icosahedral SRO (ISRO), body-centered cubic (BCC), face-centered cubic (FCC), and hexagonal close-packed (HCP) by examining the bonding around common pairs of atoms. A sequence of four integers (*ijkl*) is designed to describe the different microstructures. More information about this method can be found in Refs. [19,25–28]. The 1421 and 1422 pairs are characteristic of the bond types of FCC and HCP crystal structures in the system, respectively. The 1441 and 1661 pairs are characteristic of the bond types of BCC crystal structure.

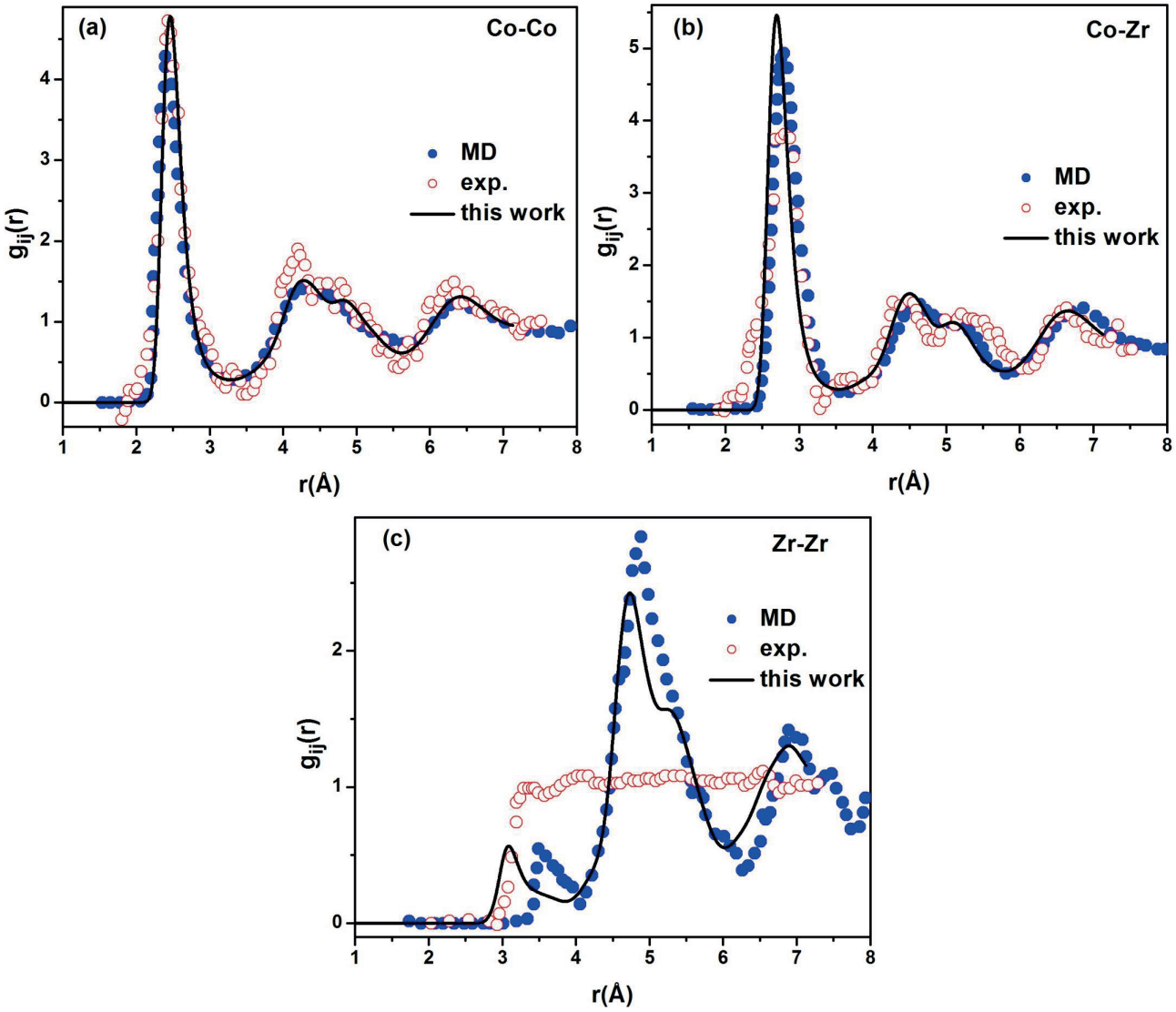

Figure 6. PRDFs of experimental [9], other MD [23], and simulated amorphous $Co_{90}Zr_{10}$ using the cooling rate of $Q_4 = 0.01$ K ps^{-1} at 300 K: (a) Co-Co pair, (b) Co-Zr pair, and (c) Zr-Zr pair.

The 1431 and 1541 bonded pairs are relative to the defective icosahedral structure in the system, while the ratio of 1551 bond type gives a measure of the degree of ISRO. Figure 7 illustrates the distribution of the HA index under four different cooling rates in the $Co_{90}Zr_{10}$ metallic glass at 300 K. It can be seen that ideal icosahedral type 1551 and defective icosahedral 1431 and 1541 types are dominant in all cooling rates, indicating the dominance of icosahedra order due to more favorable energy [29]. The 1551 bonded type is the most popular type for all cooling rates in the simulated alloy and the fraction of 1431 and 1541 bonded types decreases while the fraction of 1551 type increases as the cooling rate descends. On the other hand, the fractions of FCC, HCP, and BCC types are much less and remain almost unchanged under different cooling rates. In addition, the presence of the high fraction of 1421, 1422, 1441, and 1661 pairs denotes significant crystalline SRO in the system.

Table 2. The first peak positions r_{ij}, partial and total CNs (N_{ij}), and maximum of the first peak *G1* in the nearest-neighbor region for amorphous $Co_{90}Zr_{10}$ alloy: experimental and calculated values at 300 K.

i	j	r_{ij} [Å] This work	Exp.	N_{ij} This work	Exp.	*G1* This work	Exp.
Co	Co	2.43	2.42[a]	10.92	10.90[a]	4.78	4.71[a]
	Zr	2.71	2.79[a]	1.72	1.50[a]	5.45	3.75[a]
				12.64	12.40[a]		
Zr	Co	2.71	2.79[a]	15.47	-	5.45	3.75[a]
	Zr	3.10	-	0.33	-	0.57	-
				15.80	-		
	N_{All}	2.49	-	12.93	-	4.09	-

[a]Ref. [9].

3.5. Voronoi tessellation analysis

The Voronoi tessellation (VT) [30] analysis method is used for further classification of the polyhedral order and analysis of the SRO in the liquid and amorphous structures. This method is more sensitive than the RDF curve in determining CNs. Voronoi polyhedra (VP) are classified based on the number of edges per polyhedral faces $\langle n_3, n_4, n_5, n_6 \ldots, n_i \rangle$, where n_i is the number of i-edged polygons, offering another perspective to analyze local atomic orders. For example, the Voronoi indices of the perfect FCC, BCC, and ICOS are $\langle 0, 12, 0, 0 \rangle$, $\langle 0, 6, 0, 8 \rangle$, and $\langle 0, 0, 12, 0 \rangle$, respectively. However, the VPs in liquid and amorphous structures will be distorted from their crystalline counterparts. Although there are many coordination polyhedra types in liquid and amorphous structures, the most common 15 Voronoi indices in $Co_{90}Zr_{10}$ alloy are shown in Figure 8 for four different cooling rates at 300 K. VPs with a distribution of less than 1% are not shown. In order to better analyze the

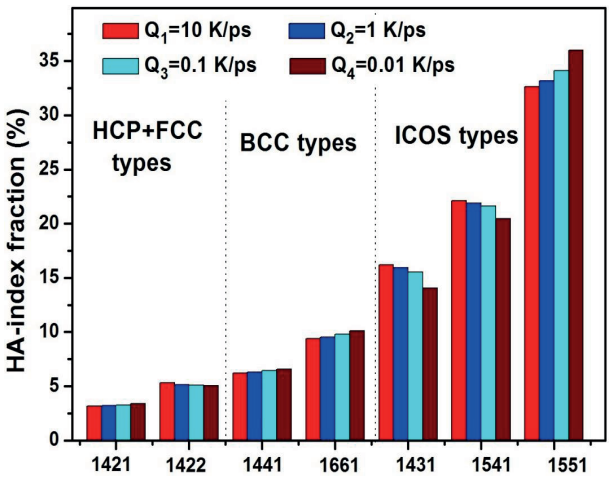

Figure 7. The distribution of the HA index under four different cooling rates in the $Co_{90}Zr_{10}$ MG at 300 K.

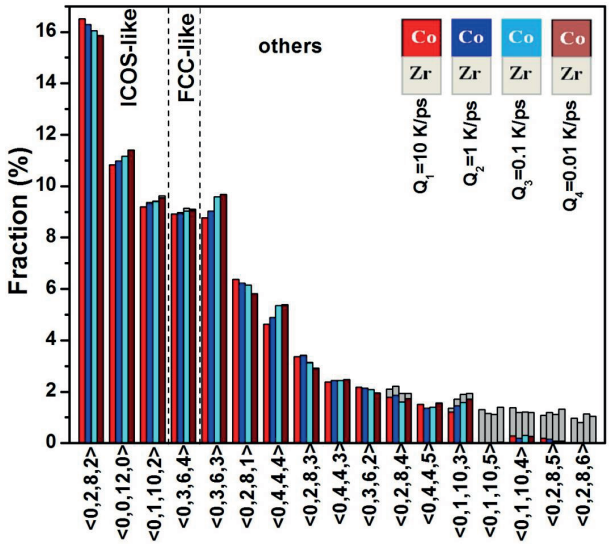

Figure 8. The fraction of the VT index under four different cooling rates in the $Co_{90}Zr_{10}$ metallic glass at 300 K.

system, we distinguished VPs within three groups. The first group is the Voronoi indices of perfect icosahedral (ICOS), $\langle 0,0,12,0 \rangle$, and distorted icosahedral (DICOS), $\langle 0,2,8,2 \rangle$ and $\langle 0,1,10,2 \rangle$. The second group consists of the Voronoi indices of the distorted FCC VP [31], such as $\langle 0,3,6,4 \rangle$, whereas the last group is composed of other common VPs. According to the results of VPs obtained for all cooling rates, ICOS-like (perfect and distorted icosahedra) and FCC-like VPs play a dominant role in the amorphous $Co_{90}Zr_{10}$ alloy. As the cooling rate slowed, perfect icosahedra $\langle 0,0,12,0 \rangle$, distorted icosahedra $\langle 0,1,10,2 \rangle$, and FCC-like $\langle 0,3,6,4 \rangle$ VPs exhibit a clearly increasing trend while distorted icosahedra $\langle 0,2,8,2 \rangle$ tend to decline. The result of the Voronoi analysis is consistent with the HA index discussed above. Interestingly, Zr-centered clusters prefer $\langle 0,1,10,5 \rangle$, $\langle 0,1,10,4 \rangle$, $\langle 0,2,8,5 \rangle$, and $\langle 0,2,8,6 \rangle$ VPs with higher CNs of ≥ 15, while Co-centered clusters prefer VPs with CNs of ≤ 14. This can reasonably be attributed to the smaller atomic radius of Co, and it can be interpreted that the Co and Zr atoms prefer to cluster with small-radius Co atoms as neighboring atoms. These results support those of the above-mentioned CNs.

Figure 9 presents the temperature-dependent evolution of ICOS-like clusters involving the polyhedra of $\langle 0,0,12,0 \rangle$, $\langle 0,2,8,2 \rangle$, and $\langle 0,1,10,2 \rangle$ during the cooling of the $Co_{90}Zr_{10}$ liquid at the cooling rate of $Q_4 = 0.01$ K ps^{-1}. It is clearly seen that the fraction of ICOS-like clusters tends to increase and there is a significant increase between the supercooled region and the T_g when the liquid is cooled from high temperatures. This sudden increase during glass transition was interpreted by Jonsson and Andersen [32] as the icosahedra ordering increasing when the average enthalpy decreases. Since the supercooled liquid transforms into glass at a temperature below the T_g ($T_g = 833$ K), its concentration reaches saturated values of about ~36% and it does not change much depending on the decreasing temperature. This fact has already been reported in many MD studies [32,33]. According to these results, it is obvious that the development of the icosahedral order plays a critical role in the glass transition of the $Co_{90}Zr_{10}$ alloy.

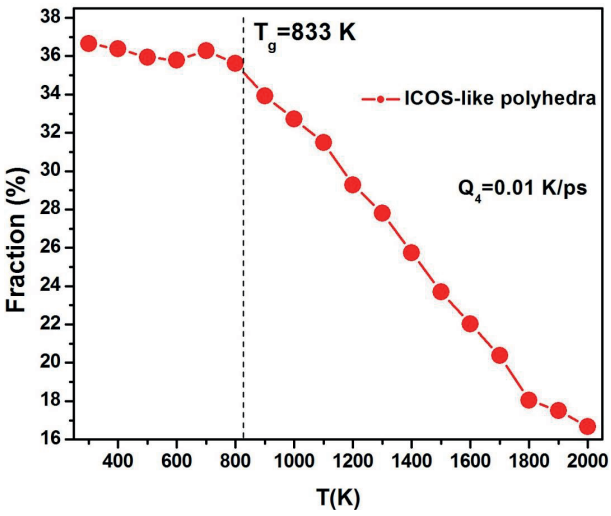

Figure 9. The evolution of the ICOS-like polyhedra with Voronoi index of $\langle 0,0,12,0 \rangle$, $\langle 0,2,8,2 \rangle$, and $\langle 0,1,10,2 \rangle$ with temperature during cooling of the $Co_{90}Zr_{10}$ liquid alloy under the cooling rate of $Q_4 = 0.01$ K ps^{-1}.

Figures 10a and 10b illustrate the temperature-dependent fraction of some dominant Co-centered and Zr-centered clusters in $Co_{90}Zr_{10}$ alloy, respectively. All common clusters in Figures 10a and 10b are depicted in Figure 11 using VESTA software for drawing the clusters [34]. As is clear in Figure 10a and 10b, Co-centered

dominant clusters are ⟨0,2,8,2⟩, ⟨0,0,12,0⟩, ⟨0,1,10,2⟩, ⟨0,3,6,3⟩, ⟨0,3,6,4⟩, and ⟨0,2,8,1⟩, and Zr-centered dominant clusters are ⟨0,1,10,5⟩, ⟨0,2,8,5⟩, ⟨0,1,10,4⟩, and ⟨0,2,8,6⟩. The Co-centered the distorted FCC VP (⟨0,3,6,4⟩) and ICOS-like VPs (⟨0,2,8,2⟩, ⟨0,0,12,0⟩, and ⟨0,1,10,2⟩) are increasing with temperature decrease. According to VT results, FCC is competing with ICOS as the temperature is lowered, and this competition is further increased by decreasing cooling rate (please see Figure 8). Interestingly, ideal icosahedra ⟨0,0,12,0⟩ for Co-centered clusters are only ~2.93% at high temperatures, while this rate increases to about ~10.73% at 300 K with decreasing temperature. These results emphasize that Co-centered VPs provide the greatest contribution to the development of the icosahedra ordering in the $Co_{90}Zr_{10}$ alloy. The fraction of Zr-centered VPs is much less than that of Co-centered VPs. On the other hand, the fractions of Zr-centered ⟨0,1,10,5⟩, ⟨0,2,8,5⟩, ⟨0,1,10,5⟩, and ⟨0,2,8,6⟩ VPs are increasing with decreasing temperature. Almost all of the Zr-centered clusters are composed of VPs with CNs of $\geq$15. This may be because Zr atoms (R_{Zr} = 1.6 Å) prefer to form clusters with Co atoms (R_{Co} = 1.25 Å), which usually have a smaller radius than themselves, as seen in the lower part of Figure 11. Similar results have been obtained with the other three cooling rates.

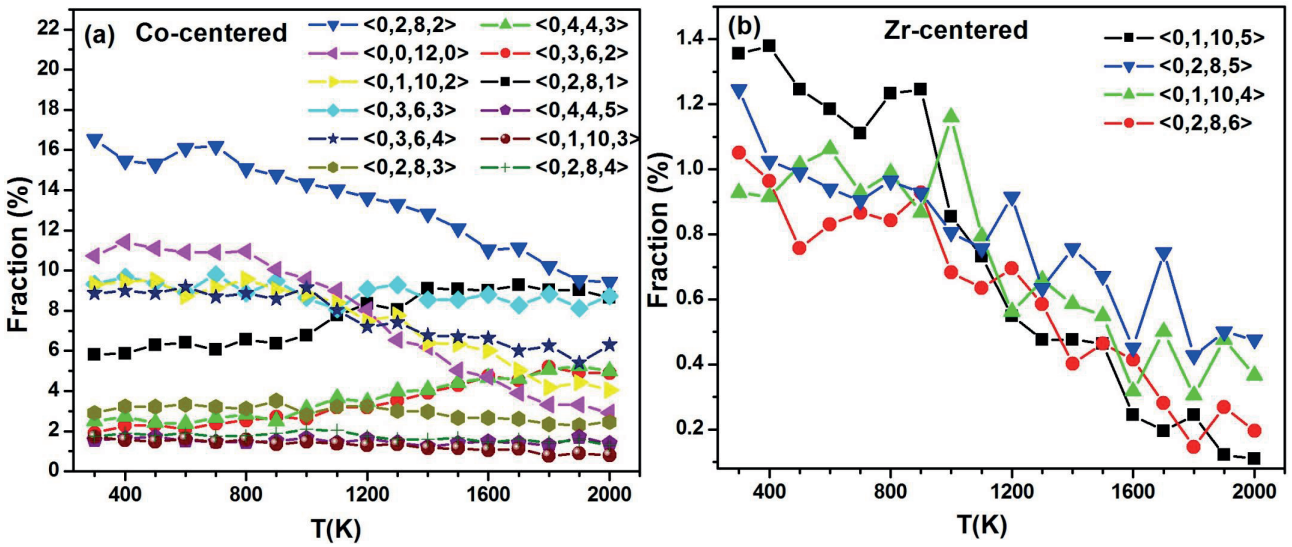

Figure 10. The fraction of the dominant Voronoi indices as a function of the temperature for (a) Co-centered and (b) Zr-centered clusters in the $Co_{90}Zr_{10}$ alloy.

4. Conclusions

To summarize, the glass formation process and the local ordered atomic structure of the $Co_{90}Zr_{10}$ alloy have been studied using MD simulations with EAM interatomic potential. Four different cooling rates of Q_1 = 10 K ps^{-1}, Q_2 = 1 K ps^{-1}, Q_3 = 0.1 K ps^{-1}, and Q_4 = 0.01 K ps^{-1} are used to investigate the effect of cooling rate on T_g and local structure. The linear variation of T_g with lgQ and the decrease in T_g with decreasing cooling rate reveal that glassy transition is indeed a typical kinetic process. That is, it has been observed that T_g is systematically decreased (from 964 K to 833 K) with decreasing cooling rate. The volume and energy values of the system have decreased with decreasing cooling rate and this is attributed to the fact that the final amorphous structure has a more closely packed structure. The calculated SF and PRDF compared well (except Zr-Zr pair) with the experimental and the theoretical results. At low temperatures a splitting is observed at

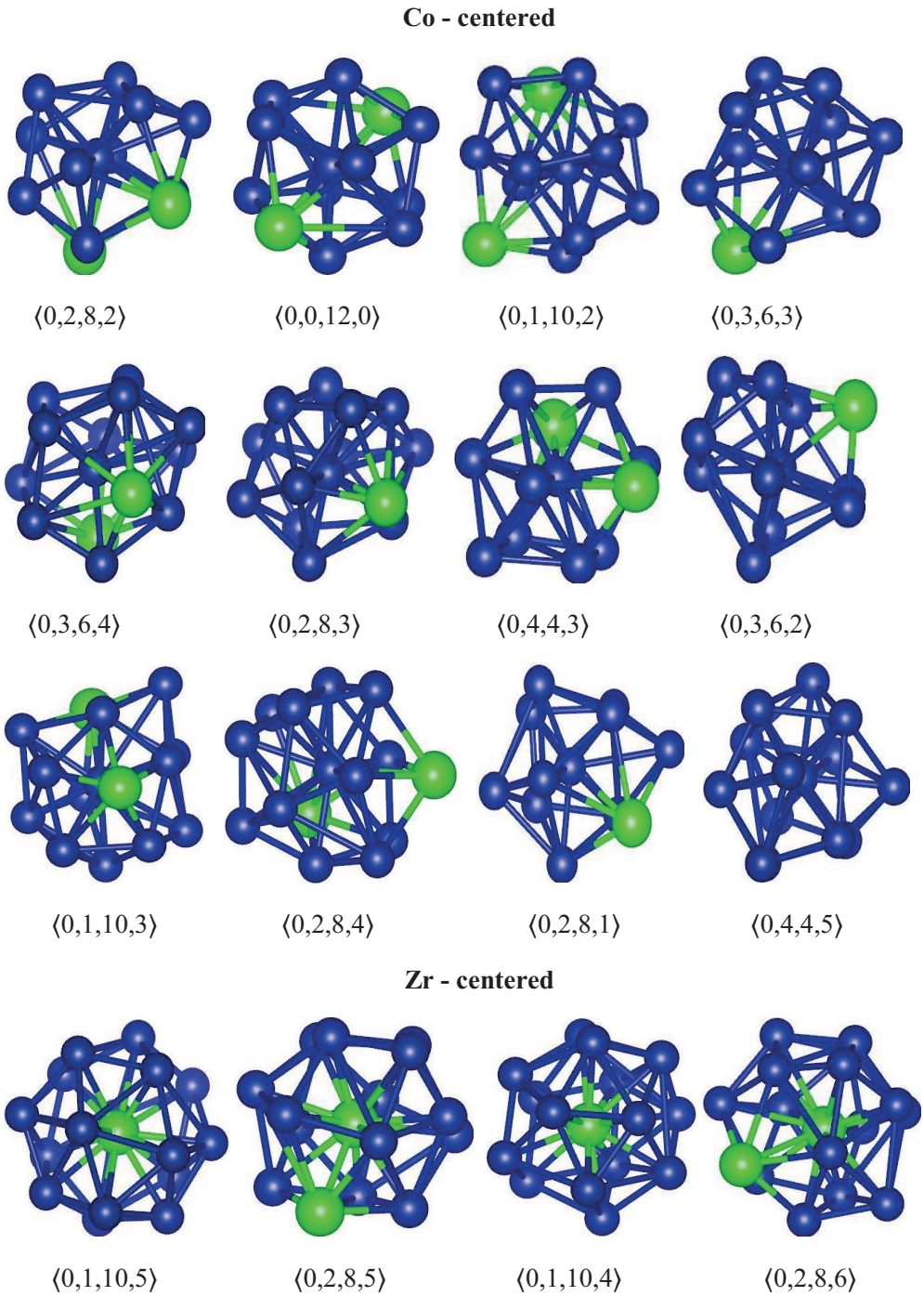

Figure 11. Representative atomic structures of the most common Co-centered and Zr-centered clusters at 300 K under the cooling rate of $Q_4 = 0.01$ K ps^{-1}. Blue and green atoms represent Co and Zr atoms, respectively.

the second maximum peaks of the SF, RDF, and PRDF curves, which is known as a characteristic feature of amorphous structures. The CNs that we calculated are in good agreement with the previously reported experimental results for the amorphous $Co_{90}Zr_{10}$ alloy. The results show that ICOS-like clusters are dominant SRO structural units at different cooling rates in amorphous $Co_{90}Zr_{10}$ alloy. According to the HA bond-pair

analysis, it has been found that a large part of the local structures of the rapidly solidified system for different cooling rates is composed of ICOS-type (1551, 1541, and 1431) pairs. Furthermore, VT analysis demonstrates that the ICOS-like clusters with indices $\langle 0,2,8,2 \rangle$, $\langle 0,0,12,0 \rangle$, and $\langle 0,1,10,2 \rangle$ are dominant. In Co-centered clusters, the distorted and perfect ICOS SRO have a high fraction; this indicates that the presence of Co plays an important role in glass formation. It is found that ICOS and FCC order increases with decreasing temperature and decreasing cooling rate. In summary, the EAM potential can be used to explain the atomic structure and the glass formation process of $Co_{90}Zr_{10}$ metallic glass.

References

[1] Chen, H. *Acta Metall.* **1974**, *22*, 1505-1511.

[2] Inoue, A. *Acta Mater.* **2000**, *48*, 279-306.

[3] Karasu, B; Yanar, A. O.; Erdoğan, O.; Kartal, S.; Ak, G.; Pirangil, S. E. *Şişecam Teknik Bülten* **2017**, *45*, 5-17 (in Turkish).

[4] Klement, W.; Willens R. H.; Duwez, P. *Nature* **1960**, *187*, 869-870.

[5] Miracle, D. B. *Nat. Mater.* **2004**, *3*, 697-702.

[6] Malozemoff, A. P.; Williams, A. R.; Terakura, K.; Moruzzi, V. L.; Fukamichi, K. *J. Magn. Magn. Mater.* **1983**, *35*, 192.

[7] Suran, G.; Naili, M.; Rivoire, M. *J. Appl. Phys.* **1990**, *67*, 5649.

[8] Mohammed Idrus, R.; Grundy, P. J. *J. Phys. D Appl. Phys.* **1986**, *19*, 1245-1255.

[9] Babanova, Y. A.; Sidorenko, A. F.; Ryazhkin, A. V.; Shvetsov, V. R.; Kronmueller, H. *Nucl. Instruments Methods Phys. Res. A* **1998**, *405*, 400-402.

[10] Saito, T. *Mater. Trans.* **2003**, *44*, 1713-1716.

[11] Daw, M. S.; Baskes, M. I. *Phsical Rev. B* **1984**, *29*, 6443-6453.

[12] Zhou, X. W.; Johnson, R. A; Wadley, H. N. G. *Phys. Rev. B* **2004**, *69*, 144113.

[13] Smith, W.; Forester, T. R. *J. Mol. Graph.* **1996**, *14*, 136-141.

[14] Zhang, Y.; Mattern, N.; Eckert, J. *J. Appl. Phys.* **2012**, *111*, 053520.

[15] Li, F.; Zhang, H.; Liu, X.; Yu, C.; Lu, Z. *Comput. Mater. Sci.* **2018**, *141*, 59-67.

[16] Cheng, Y. Q.; Sheng, H. W.; Ma, E. *Phys. Rev. B Condens. Matter Mater. Phys.* **2008**, *78*, 1-7.

[17] Cohen, M. H.; Grest, G.S. *Phys. Rev. B* **1979**, *20*, 1077-1098.

[18] Haile, J. M. *Molecular Dynamics Simulation—Elementary Methods*; John Wiley & Sons: New York, NY, USA, 1992.

[19] Sengul, S.; Celtek, M.; Domekeli, U. *Vacuum* **2017**, *136*, 20-27.

[20] Allen, M. P.; Tildesley, D. J. *Computer Simulation of Liquids*; Clarendon Press: Oxford, NY, USA, 1991.

[21] Zhang, K.; Li, H.; Li, L.; Bian, X. F. *Appl. Phys. Lett.* **2013**, *102*, 1-5.

[22] Waseda, Y. *The Structure of Non-Crystalline Materials-Liquids and Amorphous Solids.* McGraw-Hill: New York, NY, USA, 1981.

[23] Rößler, U.; Teichler, H. *Phys. Rev. E. Stat. Phys. Plasmas Fluids Relat. Interdiscip. Topics* **2000**, *61*, 394-402.

[24] Celtek, M.; Sengul, S. *Philos. Mag.* **2018**, *98*, 783-802.

[25] Honeycutt, J. D.; Andersen, H. C. *J. Phys. Chem.* **1987**, *91*, 4950-4963.

[26] Celik, F. A. *Phys. Lett. A* **2014**, *378*, 2151-2156.

[27] Celtek, M.; Sengul, S.; Domekeli, U.; Canan, C. *Eur. Phys. J. B* **2016**, *89*, 1-6.

[28] Celtek, M.; Sengul, S.; Domekeli, U. *Intermetallics* **2017**, *84*, 62-73.

[29] Doye, J. P. K.; Wales, D. J. *Science* **1996**, *271*, 484-487.

[30] Finney, J. L. *Nature* **1977**, *266*, 309-314.

[31] ten Wolde, P. R.; Ruiz-Montero, M. J.; Frenkel, D. *J. Chem. Phys.* **1996**, *104*, 9932.

[32] Jónsson, H.; Andersen, H. C. *Phys. Rev. Lett.* **1988**, *60*, 2295-2298.

[33] Wang, L.; Bian, X.; Zhang, J. *Model. Simul. Mater. Sci. Eng.* **2002**, *10*, 331-335.

[34] Momma, K.; Izumi, F. *J. Appl. Crystallogr.* **2011**, *44*, 1272-1276.